

Relationships between radiation flux and ENSO in the tropical Pacific over the last 170a

Chai Boyu (✉ 413170459@qq.com)

Guangdong Ocean University <https://orcid.org/0000-0002-8804-0028>

XU Feng

Guangdong Ocean University

XU Jian-jun

Guangdong Ocean University

HAN Li-guo

Guangdong Ocean University

CHEN Si-qi

Nanjing University of Information Science and Technology

LI Ya-jie

Guangdong Ocean University

YANG Jin-yi

Guangdong Ocean University

ZHANG Shao-jing

Guangdong Ocean University

Zheng Mei-ying

Guangdong Ocean University

LI Yong-chi

Guangdong Ocean University

Research Article

Keywords: Radiation Flux, ENSO, Typhoon, 170a

Posted Date: May 23rd, 2022

DOI: <https://doi.org/10.21203/rs.3.rs-1638018/v1>

License: © ⓘ This work is licensed under a Creative Commons Attribution 4.0 International License.

[Read Full License](#)

Relationships between radiation flux and ENSO in the tropical Pacific over the last 170a

CHAI Bo-yu^{1, 2}, XU Feng^{1, 2*}, XU Jian-jun^{1, 2}, HAN Li-guo^{1, 2}, CHEN Si-qi^{1, 2}, LI Ya-jie^{1, 2},
YANG Jin-yi^{1, 2}, ZHANG Shao-jing^{1, 2}, Zheng Mei-ying^{1, 2}, LI Yong-chi^{1, 2}

(1. College of Oceanography and Meteorology, Guangdong Ocean University, Zhanjiang 524088, China; 2. South China Sea Institute of Marine Meteorology, Guangdong Ocean University, Zhanjiang 524088, China)

Abstract: We used synthetic analysis, EOF decomposition, correlation coefficient analysis and causal analysis to investigate relationships between radiation flux and ENSO in the tropical Pacific in recent 170a. Our results indicate that SDLR increased significantly, by c.0.05 W / (M² * a), TOLR decreased slightly, by c.0.02 W / (M² * a), SDSR did not change significantly, and TISR increased slightly, by c.0.001 W / (M² * a). In the tropical western Pacific region, the average state of the tropospheric atmosphere rising and sinking intersecting area shifted eastward by 0.05 ° / a, and El Niño Modoki events increased. In the Middle East Pacific, especially Niño 3.4 with an ocean depth > 700 m, ocean heat content increased significantly, the maximum ILD region moved eastward, upward movement in the intersecting area was abnormally enhanced, the number of westerly wind bursts weakened, and the probability of El Niño Modoki occurrence increased. There was a correlation and causal relationship between marine heat content in zones Niño3 and Niño4, radiation flux, w and u, v anomalies near the intersecting zone. When the time series of the factor was ahead or behind, the lead lag correlation coefficient generally increased. The location of the ILD maximum only affected TOLR, and only SDLR can affect the longitudinal location of the ILD maximum. The longitudinal location of the ILD maximum and H_{Niño3}, H_{Niño3.4} interact as both cause and effect.

Keywords: Radiation Flux; ENSO; Typhoon; 170a

Foundation: The National Key Research and Development Program of China (2018YFA0605604); Key Research and Development Program of Guangdong Province (2020B0101130021)

Corresponding author: XU Feng, male, from Anhui province, China, professor, doctoral supervisor, engaged in atmospheric physics and atmospheric environment, marine meteorology research. E-mail: gdouxufeng@126.com

33 **1. Introduction**

34 El Niño and Southern Oscillation (ENSO) is an important air-sea coupling
35 phenomenon affecting the Pacific and even the world. One of the important variables
36 affecting ENSO is radiation, and by studying the impact of Centennial radiation flux on
37 ENSO, we can explore the impacts of weather and climate change. Predicting ENSO
38 and even global climate change trends is of great significance for the prediction of
39 extreme weather and climate events around the Pacific and even the world.

40 Meehl et al.^[1] studied the relationship between precipitation in the Intertropical
41 convergence zone (ITCZ) on the tropical Pacific and peak solar radiation, and found
42 that there was a stronger sea surface pressure difference in the peak year of solar activity,
43 which increased sea surface pressure difference between the eastern and Western
44 tropical Pacific and strengthened the trade wind, resulting in stronger ITCZ
45 precipitation in the tropical western Pacific similar to La Niña. Haigh et al.^[2] studied
46 the relationship between solar activity and atmospheric circulation and climate change
47 and found that in an enhanced solar activity year, stratosphere thermodynamic and
48 dynamic conditions were adjusted, tropospheric atmospheric circulation changed,
49 tropical precipitation strengthened and moved to the pole, and Hadley circulation range
50 expanded. This produced atmospheric circulation and precipitation distribution similar
51 to an El Niño year. Huo et al.^[3] found that El Niño Modoki will appear in the tropical
52 Pacific 1-3 years after the peak year of the solar activity cycle. Hu et al.^[4] found that
53 when an El Niño event with weak air sea coupling occurred, the SST zonal gradient in
54 the tropical Pacific was small. Seiki et al.^[5] found that under global warming, the West
55 Wind Bursts showed an upward trend in the eastern and western Pacific, and a
56 downward trend in the central Pacific and Indian Ocean, while the total number of West
57 Wind Bursts were unchanged. This may be due to increased short-term convective
58 disturbance from ocean surface temperature rises in the eastern and western Pacific.
59 Under current climate conditions, the CMIP model tends to show consistent changes in
60 the relationship between westerly outbreak and ENSO, and its simulation effect is good.
61 West Wind Bursts in the middle east Pacific are conducive to El Niño occurrence in the

62 eastern Pacific, and West Wind Bursts in the central and western Pacific are conducive
63 to El Niño occurrence in the central Pacific. Shi Yunhao et al. ^[6] pointed out that when
64 PDO was positive, westerly wind broke out more frequently in an El Niño year in the
65 east Pacific, while with negative PDO, the westerly burst in the central Pacific moved
66 westward, weakening the westerly wind burst in the central Pacific and increasing El
67 Niño Modoki. Chen Shengjie et al. ^[10] defined a new El Niño air-sea coupling index
68 according to ocean heat content, and found that when it was high, air-sea coupling was
69 strong. XZ et al. ^[13] studied the relationship between thermocline feedback and ENSO,
70 and found a positive feedback mechanism between thermocline change and El Niño
71 Modoki. Ashok et al. ^[14] defined the abnormally high SST event in the central Pacific
72 as El Niño Modoki, wherein the middle Pacific El Niño event differed from the east
73 Pacific El Niño. Yeh et al. ^[15] found that the occurrence frequency of this type of El
74 Niño may continue to rise with global warming. Moum et al. ^[16] noted that in the Niño3
75 and Niño3.4 region, there are different phases in the change of ENSO.

76 In summary, there have been some significant changes in radiation and ENSO
77 activity in the tropical Pacific in recent years. However, there has been little discussion
78 of mechanisms generating these changes. Therefore, we use a variety of statistical
79 methods, EOF decomposition, causality analysis and other methods to explore the
80 action mechanisms of radiation and ENSO related variables on the changes of ENSO
81 events in the tropical Pacific.

82 **2. Data and methods**

83 **2.1 data**

84 Through experimental comparison, it has been found that the BCC-CSM CMIP6
85 data from the Beijing Climate Centre (BCC) was best suited for radiation simulation
86 and appeared more in line with historical reality ^[7]. Therefore, we selected their data on
87 Surface Downward Longwave Radiation (SDLR), Surface Downward Shortwave
88 Radiation (SDSR), TOA Incident Shortwave Radiation (TISR), and TOA Outgoing
89 Longwave Radiation (TOLR) simulated by BCC since 1850, with a spatial resolution
90 of about $1^\circ \times 1^\circ$, and divided into 19 vertical layers. CMIP6 from NCAR was selected

91 as the vertical velocity w data since 1850, along with meridional wind (v) and zonal
92 wind (u) CMIP5 data since 1850 simulated by NCAR. The spatial resolution of u , v and
93 w data was $c.1.25^\circ \times 1^\circ$, divided into 19 vertical layers. Additionally, we used ERA5
94 data since 1950 with a spatial resolution of $0.25^\circ \times 0.25^\circ$ [8], to synthesize and analyze
95 El Niño, El Niño Modoki and La Niña events. By studying the air-sea coupling degree,
96 using NCAR's CMIP6-CESM2-historical-r11i1p1f1 SST data we calculated the heat
97 content above the ocean depth of 700 m [9, 10]. All CMIP data used were from
98 <https://esgf-node.llnl.gov/projects/>, with an initial download range of 120°E - 80°W , and
99 30°S - 30°N .

100 **2.2 Research Region**

101 Our research focused on the tropical Pacific region (120°E - 80°W , 30°S - 30°N),
102 where ocean depth is mostly >700 m, and the atmospheric height is 925-150 hPa.
103 Selected areas in the region differed in research focus, and these specific areas are
104 described in the main text.

105 **2.3 Method**

106 Firstly, we researched interdecadal changes of u - w wind and v - w wind in the
107 Pacific since 1850 and the synthetic analysis of u - w wind and v - w wind during El Niño,
108 El Niño Modoki and La Niña events. We selected the intersecting area of ascending and
109 descending motion, and calculated changes in SDLR, SDSR, TOLR and TISR, u
110 anomaly and w . Concurrently, we calculated the tropical Pacific Isothermal Layer
111 Depth (ILD) to represent ocean heat transport and distribution, then conducted wavelet
112 analysis, and calculated ocean heat content above 700 m in zones Niño3 and Niño3.4,
113 the relationship between heat content and radiation flux, u anomaly and w change in
114 the intersecting area, and researched its impact on ENSO activities. Finally, we
115 conducted a causality analysis to identify causal relationships between related variables.
116 Indication of a causal relationship between two variables are expressed by the scale of
117 the information flow between the variables (if the direction between the two variables
118 is different, the scale of the information flow will also be different). The formula to
119 determine information flow between the variables is:

120

$$T_{2 \rightarrow 1} = \frac{C_{11}C_{12}C_{2,d1} - C_{12}^2C_{1,d1}}{C_{11}^2C_{22} - C_{11}C_{12}^2}$$

121

Where C_{ij} is sample covariance between X_i and X_j . $C_{i,dj}$ is sample covariance

122

between X_i and \dot{X}_j , and:

123

$$\dot{X}_j = \frac{dX_j(n)}{dt} = \frac{X_j(n+1) - X_j(n)}{\Delta t}$$

124

The above method was used to calculate information flow between variables and

125

analyze the causal relationship between the variables [11,12].

126

3. Correlation analysis of tropical Pacific radiation and

127

related variables with ENSO in recent 170a

128

3.1 SDLR, SDSR, TISR and TOLR analysis

129

Atmospheric circulation change is related to ocean heat change, which is related

130

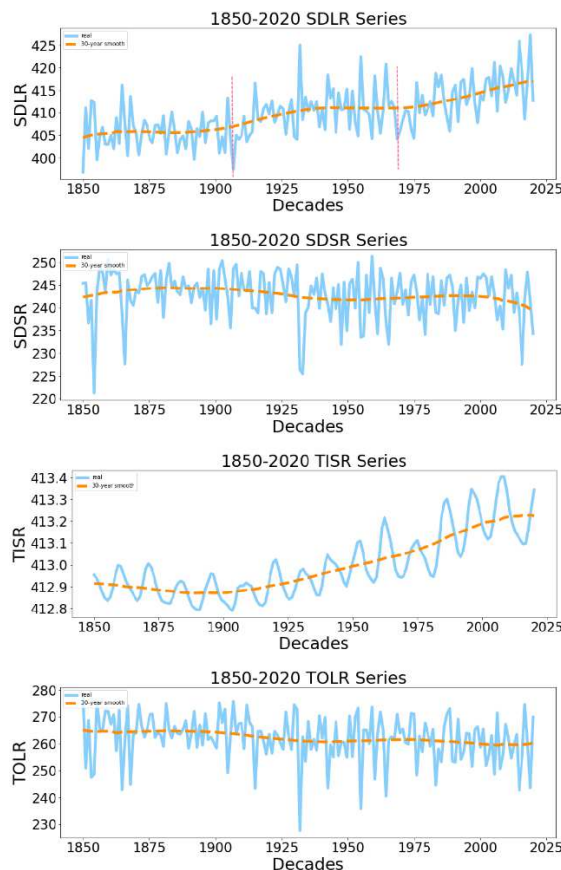
to radiation. Therefore, the interannual changes and trends of SDLR, SDSR, TISR and

131

TOLR in the intersecting area (160°E-120°W, 5° S-5°N) since 1850 were calculated

132

(Figure 1).



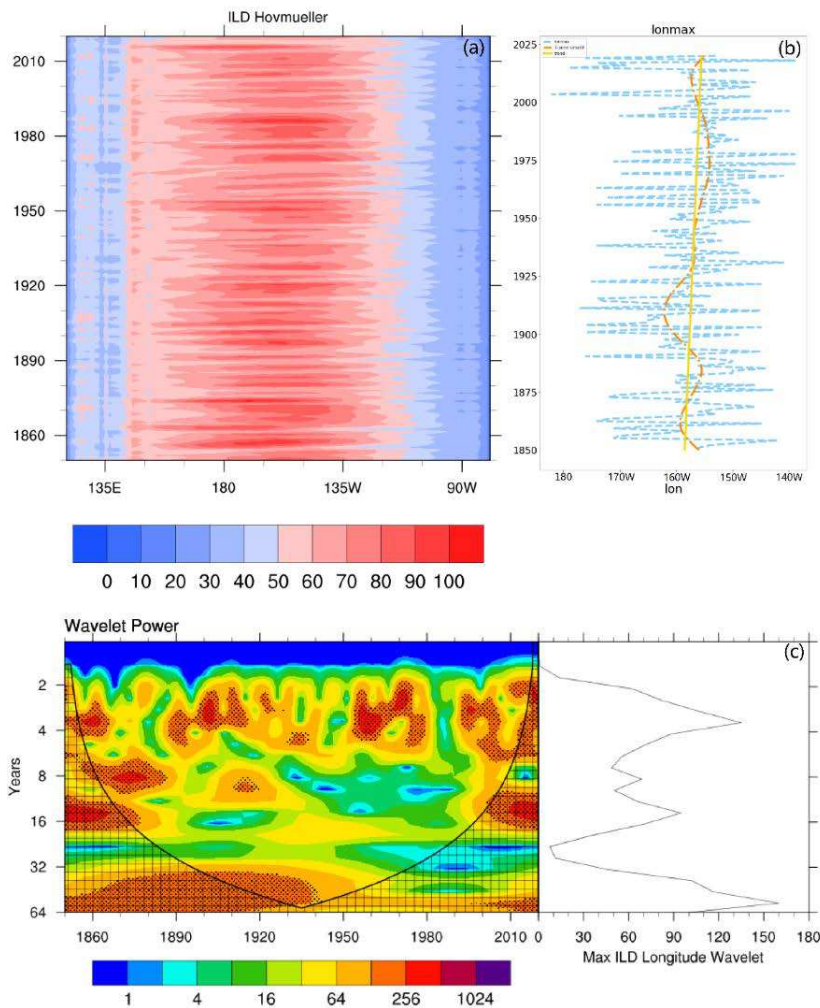
133

134 **Figure. 1** Analysis of interannual variation (blue solid line) of SDLR, SDSR, TOLR and TISR in
135 the tropical Pacific intersection area (160°E-120°W, 5°S-5°N) and trend variation after 30 years of
136 smoothing (orange dotted line) since 1850 (unit: W / m^2)

137 SDLR in the intersection area shows an increasing trend, which can be divided
138 into three parts according to the change (Figure 1). The dividing points are 1906 and
139 1968 (red dotted lines), the overall upward trend is up to $0.05 \text{ W} / (\text{M}^2 * \text{a})$, SDSR and
140 TOLR show a slight decreasing trend, with a decrease of about $0.02 \text{ W} / (\text{M}^2 * \text{a})$. The
141 frequency of SDSR minimum events increased significantly around 1930 ($\leq 235 \text{ W} /$
142 m^2), and TISR (representing the natural change of solar activity) had a slight increasing
143 trend, with an increase of about $0.001 \text{ W} / (\text{M}^2 * \text{a})$. Changing radiation flux generally
144 reflects the increase of cloud amount in the intersecting area. Notably, the increase of
145 SDLR is large, which is conducive to obtaining more energy in the intersecting area,
146 facilitating convection occurrence.

147 **3.2 Analysis of thermocline ocean heat change in recent 170a**

148 We calculated the isothermal layer depth (ILD), heat content and other variables
149 related to ocean heat change in the tropical Pacific since 1850 (Figs 2, 3).



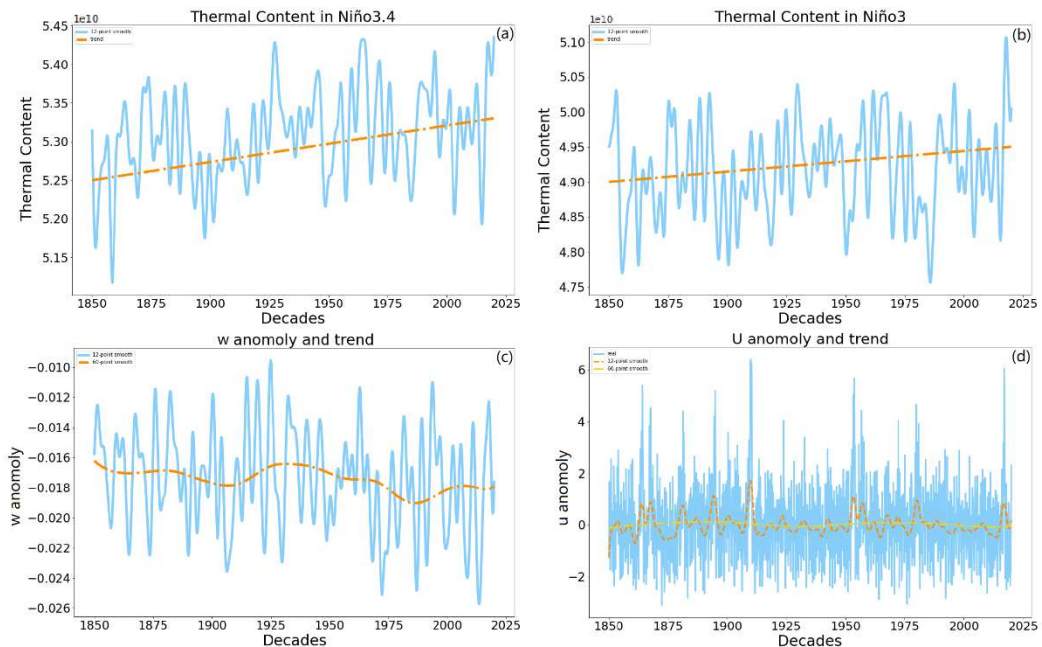
150

151 **Figure 2** (a) Hovmueller diagram of ILD in the range of 5° S- 5° n since 1850; (b) Variation in
 152 longitude of ILD maximum position (the blue line is the unsmoothed time series, the orange dotted
 153 line is the result of 12-point smoothing, and the yellow line is the change trend); (c) Wavelet analysis
 154 and power spectrum of ILD maximum position

155 Radiant heat storage in the upper ocean leads to maximum ILD in the range of
 156 170° E- 135° W, which can reach more than 80 m (Fig. 2). Additionally, maximum ILD
 157 position gradually moves eastward from 158.5° W to 155° W as shown in the trend line,
 158 and the moving rate can reach 0.1° /a. The area where maximum ILD appears is similar
 159 to the Niño3.4 zone, and its position also changes with age, which is more likely in the
 160 Niño3.4 core zone ^[13], showing that the probability of El Niño Modoki ^[14] is increasing.
 161 Furthermore, as seen from wavelet analysis, the ILD's period is significant in 4a around,
 162 which is consistent with the El Niño period. Moreover, the highest ILD longitude

163 position period shows a shortening trend, especially after 1950, indicating a significant
 164 quasi-2-4a cycle, suggesting that the probability of an El Niño Modoki event is
 165 increasing [15].

166 As large ILD can transport more heat eastward through Westerly Wind Burst, its
 167 location is so important that its correlation coefficient with ocean heat content in the
 168 tropical middle east Pacific can reach about 0.7. ENSO change is related to the degree
 169 of air-sea interaction, which is related to ocean heat content, westerly burst and vertical
 170 velocity [10]. To gain a deeper understanding of the Niño3.4 and Niño3 zones and the
 171 degree of air-sea interaction, we calculated ocean heat content above 700 m in the
 172 Niño3.4 and Niño3 zones and defined them as HNiño3.4 and HNiño3, and calculated
 173 the west wind anomaly in the intersecting area since 1850 (which is defined as u). The
 174 vertical velocity anomaly between 10°S and 10°N of the intersecting area was also
 175 calculated, and defined as w (in the distribution and change diagram of the mean state
 176 of vertical motion in each year in Fig. 6, the upward motion is mainly distributed in
 177 10°S-10°N, so the calculation range of w is between 10°S-10°N) (Fig. 3).



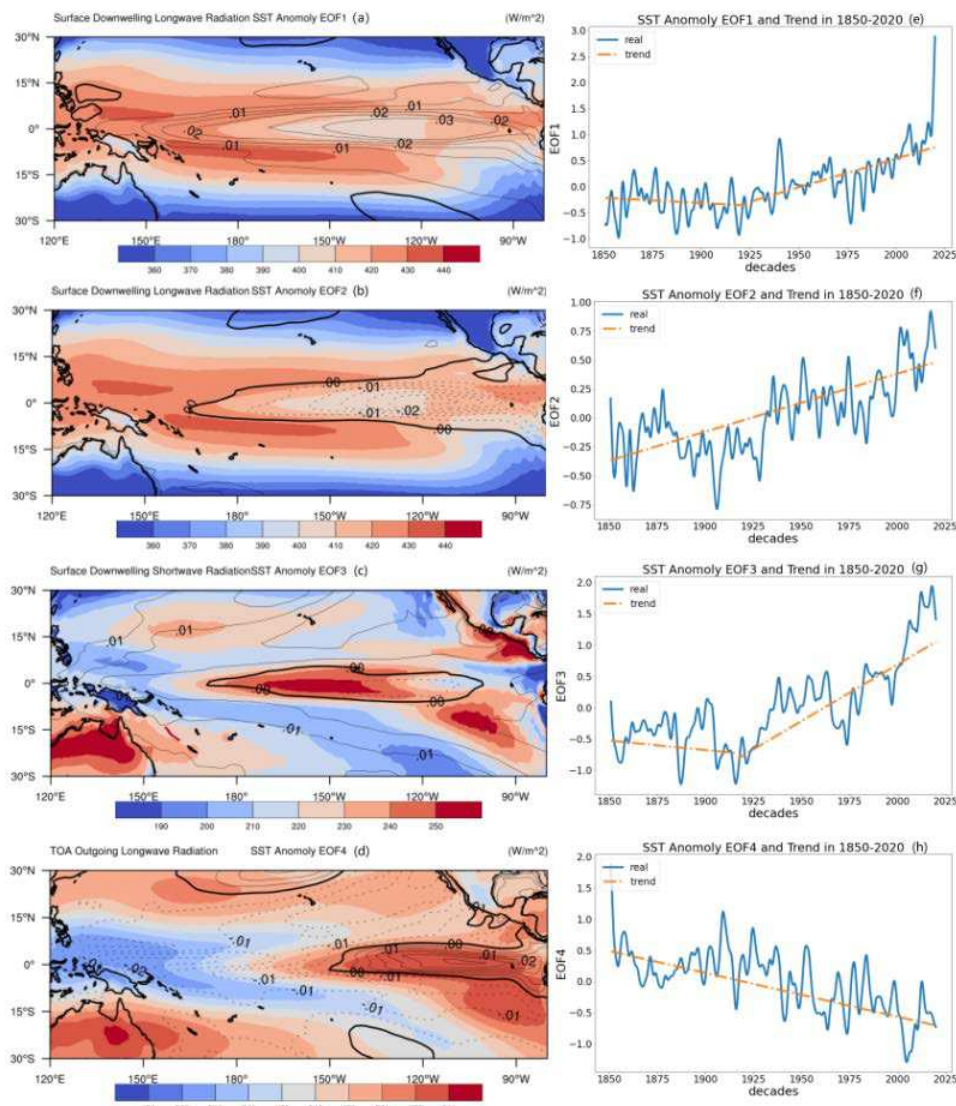
178
 179 **Figure 3** Variation (blue) and trend (orange) in ocean heat content (unit: W/m^2) in (a) the Niño3.4
 180 zone and (b) the Niño3 zone above 700 m smoothed by 12 points from 1850 to 2020, (c) the average
 181 vertical velocity field smoothed by 12 points (annual smoothing, blue) and 60 points (5a smoothing,
 182 orange) in the range of 10°S-10°N (w downward is positive) and (d) zonal wind anomaly field (u

183 westerly is positive, and the variation is blue, orange is smoothed after 12 points, and yellow is
 184 smoothed after 60 points)

185 Ocean heat content clearly increased in the Niño3.4 zone, and increased slightly
 186 in the Niño3 zone, indicating that ocean heat change in the Niño3.4 zone produced a
 187 more obvious and intense air-sea coupling (Fig. 3) [10]. It also shows that the probability
 188 of El Niño Modoki is increasing [15]. Concurrently, in the intersecting area, the updraft
 189 tends to become stronger, the westerly wind anomaly decreases slightly with time, and
 190 the frequency of Westerly Wind Bursts decreases, also indicating that the probability of
 191 El Niño Modoki is increasing [17].

192 3.3 EOF decomposition of SST anomaly and radiation synthesis

193 analysis in recent 170a



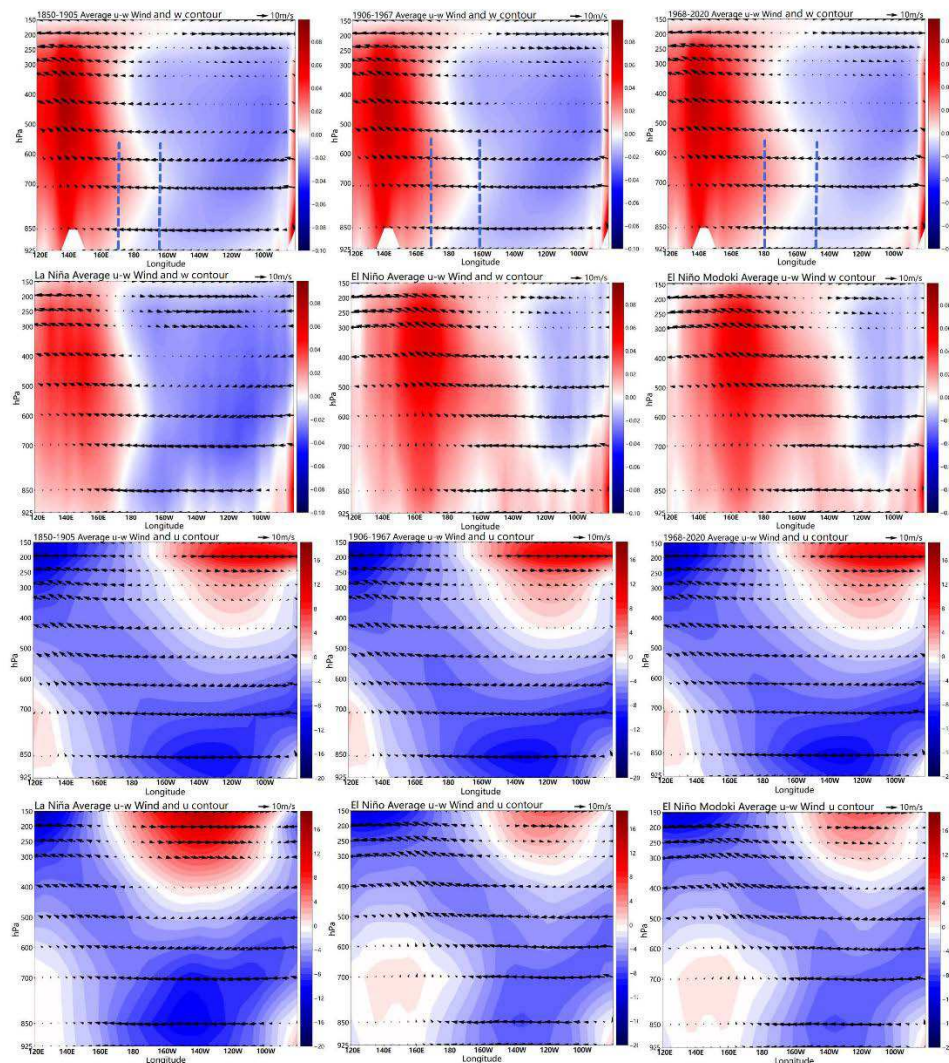
195 **Figure 4** SDLR, SDSR and TOLR distribution in the tropical Pacific and EOF analysis results of
196 SST anomaly with seasonal signal removed (EOF spatial model is represented by solid line for
197 positive value, dotted line for negative value, and 0 line is thickened. EOF time model is represented
198 by solid blue line, and its trend is represented by a dotted orange line). The (a) and (b) contours are
199 170a SDLR spatial mean field distribution. The line shows the spatial distribution of the first and
200 second modes of EOF in the near 170a Pacific SST anomaly. The (c) contour is the SDSR spatial
201 mean field distribution near 170a mean, and the line shows the spatial distribution of near 170a
202 Pacific SST anomaly third model. The (d) contour shows the spatial mean field distribution of TOLR
203 in recent 170a, and the line shows the spatial distribution of the fourth mode of SST anomaly in
204 recent 170a. (e), (f), (g), and (h) are the time series and trends of the first to fourth EOF modes in
205 the Pacific SST anomaly in recent 170a.

206 The first, second, third and fourth EOF decomposition modes of Pacific SST
207 anomaly have obvious corresponding relationships with radiation flux SDLR, SDSR
208 and TOLR, and the positive or negative center of each mode coincides with the positive
209 or negative center of each radiation flux on the low latitude region (Fig. 4). The SDLR
210 distribution in the east equatorial Pacific is smaller than in the west, while the centers
211 of the first and second modes of the SST anomaly are located in the Niño3 zone of the
212 eastern Pacific. This region has the smaller SDLR on the equator, the positive center in
213 the first mode of the eastern Pacific, and the negative center in the second mode. SDSR
214 distribution is small in the west and large in the east of the equatorial Pacific, the high
215 value center is located in the Niño3.4 zone, the third SST mode of anomaly is dominated
216 positive, but there is a large negative area in the equatorial Pacific. The negative center
217 is also located in the Niño3.4 zone, corresponding to the center of SDSR high value.
218 TOLR distribution is at its lowest in the west and highest in the east of the equatorial
219 Pacific. The fourth SST mode of anomaly has a large gradient on the equator, the
220 positive value center is located in the Eastern Pacific, and the negative value center is
221 located in the western Pacific, which corresponds to large and small TOLR distributions.

222 **3.4 Synthetic analysis of mean atmospheric circulation flow**

223 Since Niño1, Niño2, Niño3, Niño3.4, Niño4 and the rising area of atmospheric

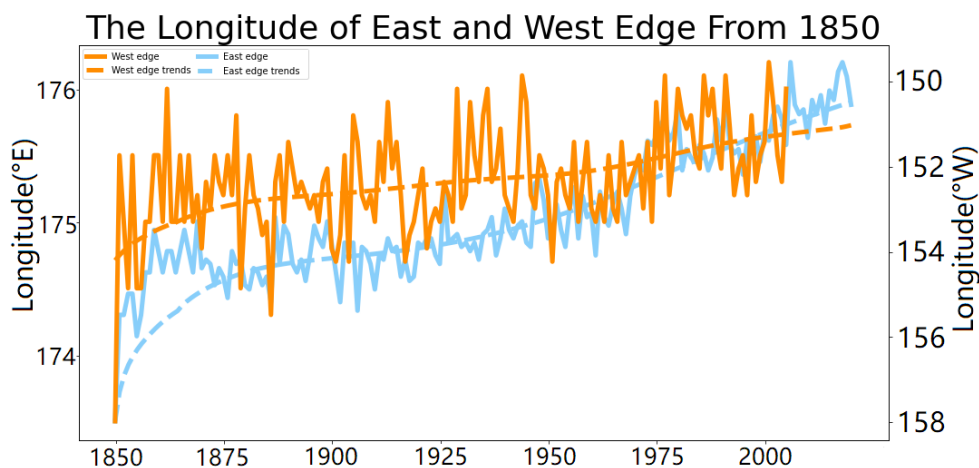
224 movement in the tropical western Pacific are included in the range of 120°E - 80°W
 225 and 5°S-5°N, and they are closely related to ENSO. To explore the average state change
 226 of circulation in the tropical Pacific and the change of atmospheric circulation of ENSO
 227 activity, we set the SDLR change boundary points as 1906 and 1968. Then, we divided
 228 the distribution of u-w wind into three stages using boundary points between 120°E-
 229 80°W under the meridional average of 5°S-5°N and calculated u-w wind for El Niño,
 230 El Niño Modoki and La Niña events since 1950. The background contour was divided
 231 into two cases of w and u, and a total of 12 average states are discussed, respectively
 232 (Fig. 5 and Fig. 7).



233
 234 **Figure. 5** Synthetic analysis of average state of u-w wind in each year between 120°E-80°W with
 235 meridional average of 5°S-5°N (the boundary of each stage is defined according to the boundary
 236 point of SDLR in Fig. 1) and u-w wind for La Niña, El Niño and El Niño Modoki events since 1950.

237 The blue dotted line in the u-w wind diagram represents the east and west edge longitude position
 238 of the intersection of updraft and downdraft area in the climate average state (contour is the
 239 background field w and u respectively)

240 In the tropical Pacific west of the international date line, the low-level is mainly east
 241 wind and the high-level is mainly west wind, while in the tropical Pacific east of the
 242 international date line, the lower layer is weak westerly transmission, and the upper
 243 layer is mainly easterly transmission (Fig. 5). When a La Niña event occurred, the
 244 Walker circulation east of the international date line increased and the range extended
 245 eastward, the westerly transmission in the lower layer of the region disappeared, and
 246 the lower layer became easterly transmission. Downdraft prevails in the east near the
 247 international date line, and ascending prevails in the west. There is an interactive belt
 248 of ascending and descending movement which varies in height, with ascending
 249 movement that reaches the easternmost near 700 hPa. In each mean state, there is an
 250 obvious intersecting area of upward and downward movement. In a La Niña event
 251 synthetic state, the intersecting area is significantly west of the mean state, while in El
 252 Niño and El Niño Modoki synthetic states, the intersecting area is significantly east
 253 compared to mean state, the intersecting area below 850 hPa is not obvious, and there
 254 is no obvious downward movement.

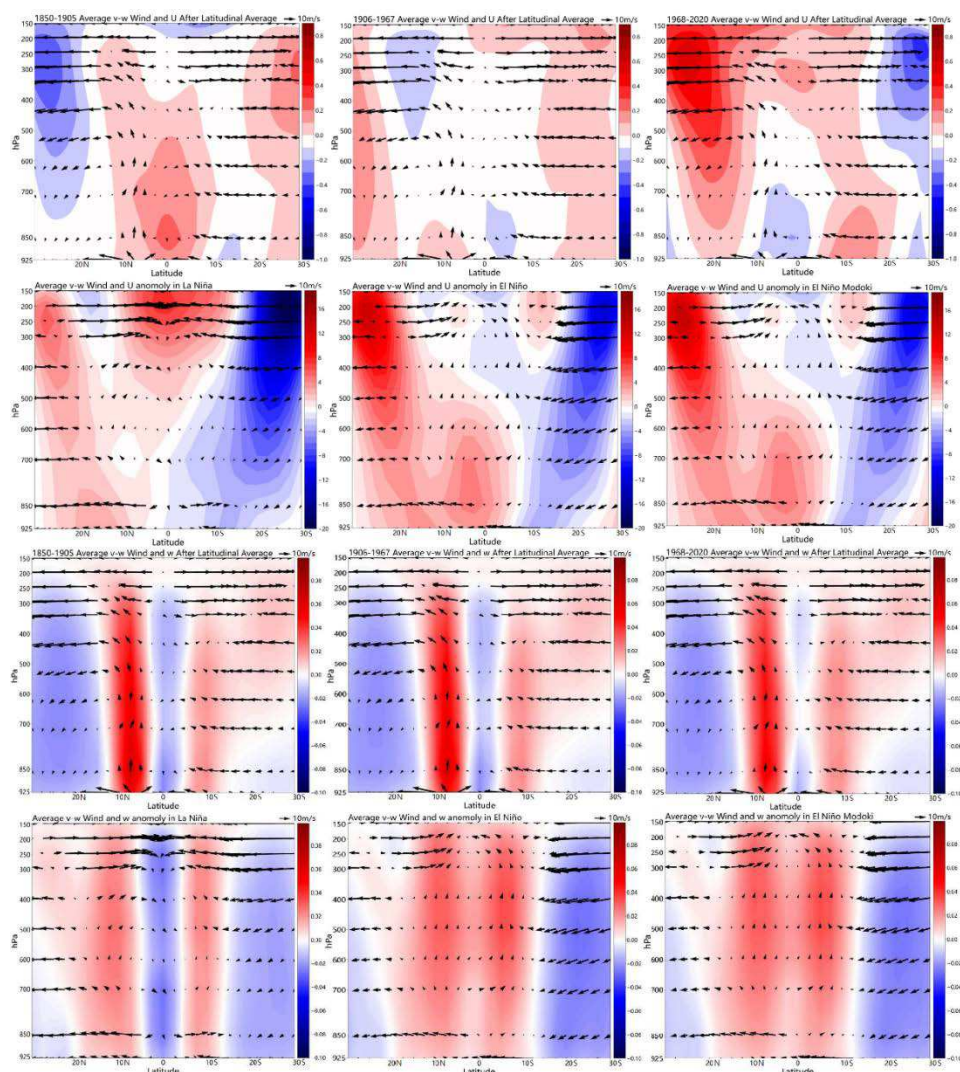


255
 256 **Figure. 6** Longitudinal changes in the east (blue) and west (orange) boundaries of the intersection
 257 area (taking the average vertical velocity equal ± 0.01 m/s as the boundary of the intersection area)

258 The rising side of the intersection area advances eastward over time, with a speed
 259 of about $0.05^\circ/a$ (Fig. 6). In the central Pacific, the upward movement of El Niño

260 Modoki's synthetic field is more obvious than that of El Niño (Fig. 5). When the average
 261 state of the intersection area of each decade moves eastward, it is more conducive to
 262 the outbreak of an El Niño Modoki event.

263 We defined the intersection position (near 160 ° E) of the movement of La Niña in
 264 Fig. 5 as the west boundary of the intersection area, and the intersection position (near
 265 120°W) of the rising and sinking movement of El Niño in Fig. 5 as the east boundary
 266 of the intersection area. Therefore, the intersection area is located near the equator at
 267 160°E-120°W, and later we conduct a correlation analysis of the related variables in
 268 this area.



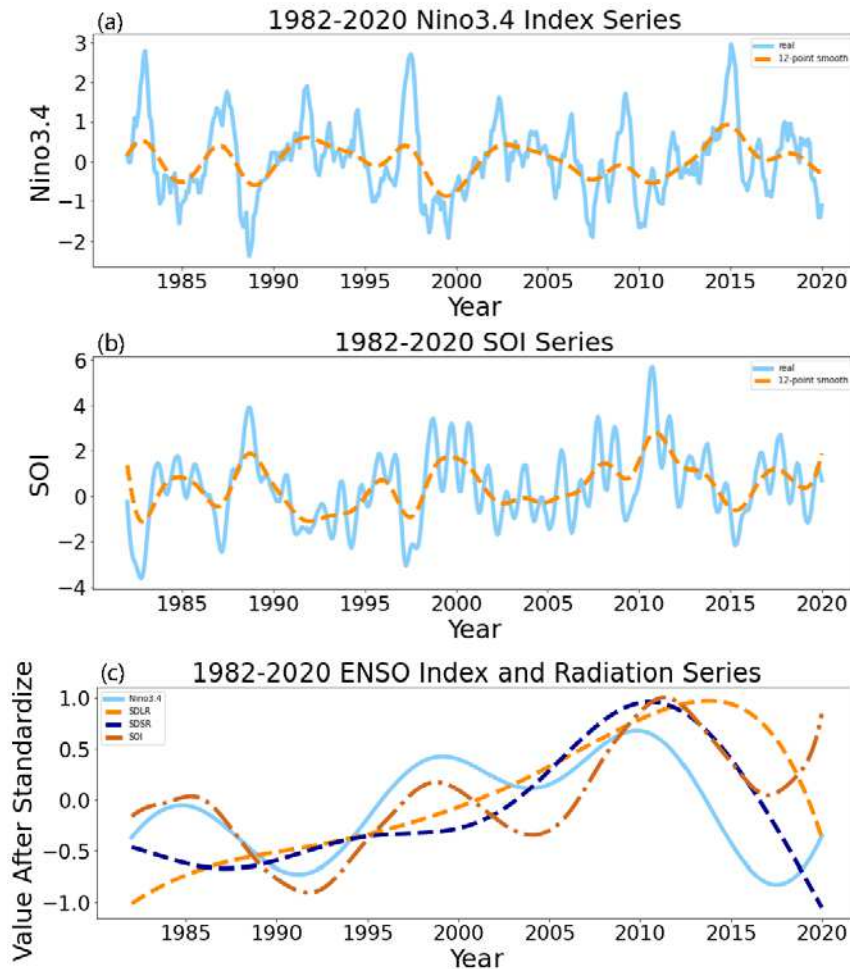
269
 270 **Figure. 7** Distribution of v-w wind in the intersection area divided by boundary points in Fig.1 from
 271 30°S-30°N zonal average and the synthetic analysis (vector field) of v-w wind for La Niña, El Niño
 272 and El Niño Modoki events since 1950, as well as the zonal average of zonal wind (u) anomaly and

273 vertical wind (w) anomaly in this area (contour field).

274 For the distribution of the average state in various years, upward movement is
275 mainly distributed between 10°S - 10°N (Fig. 7). In the contour diagram, a positive value
276 represents the westerly (upward) movement anomaly and a negative value represents
277 the easterly (downward) movement anomaly. For the average states in this region, the
278 westerly anomaly in the middle and lower troposphere tends to weaken, which is not
279 conducive to the eastward transportation of warm seawater to the central Pacific, nor to
280 the generation of the east Pacific El Niño, resulting in their reduction. At the same time,
281 zonal wind anomaly field changes near the equator in every stage from the distribution
282 situations of the El Niño and La Niña events, may also increase the probability of a La
283 Niña event. The mean state shows that there is a sinking anomaly on the equator, and a
284 strong rising anomaly on both sides of the equator, especially in the northern
285 hemisphere, which corresponds to the previous double ITCZ theory and the conclusion
286 that the ITCZ in the northern hemisphere is stronger. Moreover, in a La Niña year, the
287 equatorial downward anomaly is abnormally strong, while in an El Niño, the equatorial
288 downward anomaly disappears and becomes an upward anomaly.

289 **3.5 Analysis of ENSO index variety**

290 Since the NOAA CPC publication shows that the Niño3.4 index is directly related
291 to El Niño Modoki events ^[14]. To verify the conclusion above, we use the Niño3.4 and
292 SOI index since 1982 to 2020 from NOAA CPC monthly data, then we selected and
293 standardized the SDLR and SDSR time series since 1982 as well, and compared them
294 to the Niño3.4 and SOI index.



295

296 **Figure 8** (a) Niño3.4 index (b) SOI index and, (c) ENSO index from 1982-2020 after 12 points
 297 smoothing; and their trend's with radiation flux SDLR, SDSR after 60 points smoothing

298 Since 1982, the Niño3.4 and SOI indices tended to fluctuate, and the relative
 299 maximum value of the Niño3.4 index appeared three times, of which the absolute
 300 maximum value appeared around 2015 (Fig. 8). The SOI index increased slightly since
 301 1982, which has a high correlation with the eastern Pacific type El Niño. When the SOI
 302 index becomes negative, it is conducive to the formation of the eastern Pacific type El
 303 Niño. Changing trends in the Niño3. 4 and SOI indices are conducive to the occurrence
 304 of El Niño Modoki and the decrease of El Niño in the eastern Pacific ^[17]. Trend changes
 305 in SDLR, SDSR with the Niño3.4 and SOI indices are similar, the correlation
 306 coefficient of SDLR and Niño3.4 index reached 0.3328, SDLR and SOI reached 0.2965,
 307 the correlation coefficient of SDSR and Niño3.4 index reached 0.6255 and that of SOI
 308 reached 0.2865. Changing trends in the four indices were relatively consistent.

4 Correlation Analysis

4.1 correlation coefficient and Lead-Lag analysis between heat content and radiation

We calculated correlation coefficients between SDLR, SDSR, TOLR, TISR and Niño3 zone, Niño3.4 zone ocean heat content above 700 m (Table 1).

Table 1 Correlation coefficients between radiation flux and marine heat content in Niño3 and

	Niño3.4 areas	
	$h_{Niño3.4}$	$h_{Niño3}$
SDLR	0.1031**	0.1034**
SDSR	-0.1987**	-0.2097**
TOLR	-0.0746*	-0.0463
TISR	0.0637*	0.013

Note: * represents $P < 0.05$, ** $P < 0.001$

SDLR was positively correlated with heat content in the Niño3.4 and Niño3 areas (Table 1). In contrast, SDSR, TOLR were negatively correlated with heat content, and the relationship of SDSR and heat content was more powerful. Moreover, the relationship between SDSR and heat content in Niño3 was stronger than in Niño3.4, perhaps because SDSR provides the obvious heat content in the east of the intersection area, also there is hysteresis. The correlation between TOLR and heat content in the Niño3.4 zone is stronger than in the Niño3 zone, which may be due to greater cloud cover in the former, and a greater vulnerability to precipitation. Similarly, the correlation coefficient between TISR and heat content was statistically significant only in Niño3.4, which shows that natural levels of solar radiation can also heat the upper ocean there. Alternatively, the weak correlation between TISR, TOLR and heat content in the Niño3 zone may be due to the inverse phase relationship between the convergence ascending motion anomaly in the Niño3.4 and Niño3 zones ^[16].

333 Table 2 Lead-lag correlation of marine heat content and radiation in the Niño3 and Niño3.4 zones

	$h_{Ni\acute{o}3.4}$ (Heat content lags for 6 months)	$h_{Ni\acute{o}3}$
SDLR	0.1371**	0.1622** (Heat content lags for 1 month)
SDSR	-0.1773**	-0.0784* (Heat content lags for 1 month)
TOLR	-0.0823**	-0.0628* (Heat content 6 months ahead)
TISR	-0.0184	-0.0190 (Heat content 6 months ahead)

334 Note: * represents $P < 0.05$, ** $P < 0.001$

335 In the Niño3.4 zone, the correlation of heat content lagging behind radiation for 6
 336 months reached a maximum, while in the Niño3 zone, the correlation of heat content
 337 lagging behind SDLR for 1 month reached a maximum and leading TOLR for 6 months
 338 reached the maximum (Table 2). SDLR had a positive effect on heat content, while
 339 SDSR and TOLR had a negative effect. Except for TISR, other radiation fluxes had
 340 statistically significant lead-lag correlations with ocean heat content.

341 **4.2 Correlation coefficient and lead-lag analysis between radiation and** 342 **vertical wind, zonal wind in the intersection area**

343 In a particular ocean area, when SST and heat content are high, it facilitates the
 344 convergence and upward movement of the surface atmosphere, and therefore radiation
 345 flux is one of the important ways for the ocean to obtain heat. So in the intersection area
 346 of the Pacific Ocean, radiation flux above the ocean may affect vertical velocity and
 347 ocean heat content. To investigate this further, we calculated the correlation coefficients
 348 between vertical velocity and radiation flux (Table 3) and ocean heat content (Table 4)
 349 in the intersection area from 1850 to 2020.

350 Table 3 Lead-lag correlation coefficients between each radiation and vertical velocity
 351 (w) in the intersection area

	w	w(lead-lag)
SDLR	-0.0445	-0.08* (w lags for 5 months)
SDSR	0.3386**	-0.2164** (w lags for 3 months)
TOLR	0.0431	-0.2586** (w 1 month ahead)
TISR	0.0336	-0.1132* (w lags for 5 months)

Note: * represents $P < 0.05$, ** $P < 0.001$

The correlation between SDSR and w was strongest in the intersection area (Table 3). When SDSR increases for 3 months, the increased energy absorbed by the sea surface and the increase in evaporation promotes the development of rising motion. Therefore, when w lags behind for 3 months, the correlation coefficient between them becomes significantly negative. When w lagged behind SDLR, TOLR and TISR, the correlations between increased SDLR, TOLR, TISR and w were all statistically significant, indicating that radiation changes before atmospheric vertical movement in the equatorial Pacific.

Table.4 Lead-lag correlation coefficients between ocean heat content in the Niño3, and Niño3.4 zones and vertical velocity (w) in the intersection area

	w	w (lead-lag)
$h_{\text{Niño}3.4}$	0.0083	-0.064*(w lags for 10 months)
$h_{\text{Niño}3}$	-0.0144	0.0803*(w lags for 13 months)

Note: * represents $P < 0.05$, ** $P < 0.001$

In the intersection area, there was no obvious relationship between ocean heat content in the Niño3 and Niño3.4 zones and vertical velocity, but when w lagged 10 months, the increase (decrease) of ocean heat content in zone Niño3.4 was significantly related to the rising (sinking) movement (Table 4). When w lagged behind for 13 months, the increase (decrease) of ocean heat content in the Niño3 area was also significantly related to the sinking (rise) movement in the intersection area. This shows that after the increase in ocean heat content in zone Niño3.4, heat transfer to the atmosphere was conducive to the development of convergence and upward movement in the area above and to the east, but the signal transmission speed was slow. The upward movement in the intersection area and the heat content change in the Niño3 and Niño3.4 zones may have an inverse phase relationship, which is consistent with the above conclusion.

The burst of westerly winds is an important indicator of convergence and upward movement in many regions of the tropical ocean, and is also an important way of heat

378 transfer in the equatorial Pacific ^[17]. Therefore, the Westerly Wind Burst is also one of
 379 the important indicators of ENSO occurrence and development. When the Westerly
 380 Wind Burst occurs in the intersection area, it would therefore be easy to transport central
 381 and western Pacific seawater with high heat content to the east. To explore this
 382 possibility, we calculated the lead-lag correlation coefficients between radiation and
 383 westerly wind anomaly (Table 5).

384 Table 5 Lead-lag correlations between west wind anomaly and radiation flux in the
 385 intersection area

	U	u(lead-lag)
SDLR	0.0345	-0.2596**(u lags for 3 months)
SDSR	0.2984**	0.4831**(u lags for 1 month)
TOLR	-0.1112**	-0.2530**(u 2 months ahead)
TISR	0.0336	0.0025(u lags for 3 months)

386 Note: * represents P<0.05, ** P<0.001

387 The correlation between SDSR and west wind anomaly was strongly significant
 388 (Table 5). When the intersection area West Wind Burst lagged behind SDSR by one
 389 month, the correlation coefficient reached 0.4831, which indicates that enhanced
 390 shortwave radiation in the equatorial Central Pacific may lead to a warm and low-
 391 pressure anomaly in the central Pacific region, forming a pressure gradient anomaly
 392 with the west, which is conducive to an eastward westerly wind anomaly increase. The
 393 relationship between TOLR and west wind anomaly is also strong but different, because
 394 when the westerly anomaly is two months ahead of TOLR, the correlation is strongest,
 395 because the west wind anomaly in the equatorial Indian Ocean and Pacific warm water
 396 region can promote the transmission of convective signals to the East. The decrease
 397 (increase) of TOLR is related to the increase (decrease) of cloud caused by convergence
 398 rising (divergence sinking) ^[18]. SDLR is significantly correlated only when the westerly
 399 anomaly lags three months. The relationship between the natural variability of solar
 400 radiation (TISR) and the westerly anomaly was non-significant, which may be because
 401 the variation range was small.

4.3 Causality analysis

To clarify the relationships between radiation flux and vertical wind, zonal wind, heat content and other variables in the intersection area and the location of maximum ILD, we used the causal analysis method outlined in Liang [11,12]. Since the causal relationships between TISR and w, u were non-significant, the relationship between TISR and other related variables was relatively weak, and there was no obvious corresponding relationship with the EOF mode of SST anomaly, and so only SDLR, SDSR and TOLR were used for radiation flux in the causality analysis. As the time series used is long and the probability of passing the test is high, only variables significant at $P < 0.001$ were selected to determine causal relationships between variables.

Table 6 Causality analysis among ENSO related variables

	SDLR	SDSR	TOLR	w	u	$h_{\text{Niño}3}$	$h_{\text{Niño}3.4}$	Max ILD lon
SDLR		0.1111*(0.0179)	0.1840*(0.0658)	0.0023*(0.0020)	0.0054*(0.0017)	0.0033*(0.0026)	9.08E-04	0.0010*(0.0009)
SDSR	0.1294*(0.0088)		0.1743*(0.0155)	0.0365*(0.0156)	0.1052*(0.0142)	0.0228*(0.0053)	0.0159*(0.0047)	0.006
TOLR	3.06E-04	0.1361*(0.0220)		0.0025*(0.0024)	0.0134*(0.0041)	0.0039*(0.0024)	0.0012	0.0028
w	0.0052*(0.0012)	0.0157	0.0073*(0.0019)		0.0210*(0.0039)	0.0047*(0.0032)	0.0062*(0.0033)	3.70E-05
u	0.0032*(0.0032)	0.0820*(0.0132)	0.0137*(0.0029)	0.0212*(0.0035)		0.0018	0.0096*(0.0015)	0.0016
$h_{\text{Niño}3}$	0.0066*(0.0030)	0.0057*(0.0103)	0.0077*(0.0036)	0.0076*(0.0059)	0.0175*(0.0047)		0.2171*(0.0578)	0.1585*(0.1213)
$h_{\text{Niño}3.4}$	0.0019*(0.0012)	0.0024	0.0035*(0.0021)	0.0055	0.0104*(0.0033)	0.285*(0.056)		0.1539*(0.1334)
Max ILD lon	0.0005	0.0055	0.0031*(0.0028)	-0.00014864	0.0009	0.0978*(0.0925)	0.1005*(0.0856)	

Note: numbers in parentheses represent the information flow size threshold for $P < 0.001$; *

represents $P < 0.05$, ** $P < 0.001$

In the intersection area, there was a causal relationship between the 3 kinds of radiation and other variables, except for TOLR which little impact on SDLR. Moreover, except for SDLR and TOLR to $h_{\text{Niño}3.4}$, w and $h_{\text{Niño}3.4}$ to SDSR, information flows failed to pass the test. The other information flows passed the test, which shows that except for the variables represented by the direction of the above information flows, the three kinds of radiation flux and w, u, $h_{\text{Niño}3}$, $h_{\text{Niño}3.4}$ have mutual cause and effect.

422 Similarly, besides w , u , Hnño3 and Hnño3.4, which characterize ENSO activity
423 between these four variables, except u to Hnño3 and Hnño3.4 to w 's information flow
424 fails to pass the test, there is a mutual causal relationship between other variables. The
425 ILD maximum longitudinal position will only affect TOLR, and only SDLR can affect
426 its position, although the ILD maximum longitude position and Hnño3, Hnño3.4 have
427 a mutual causal relationship, which shows that ILD location is closely related to ocean
428 heat, which then affects the circulation situation in the equatorial Pacific.

429 **5 Discussion and conclusions**

430 1. In the past 170 years, the mean state of the intersection area has moved eastward
431 by $0.05^\circ/a$, and its upward movement near the equator has strengthened, which has been
432 conducive to the occurrence of El Niño Modoki and energy accumulation zone Niño3.4.

433 2. In recent 170a, SDLR increased significantly in the intersection area, up to 0.05
434 $W / (M^2 * a)$, TOLR decreased slightly, about $0.02 W / (M^2 * a)$, SDSR did not change
435 significantly, and longitude of the ILD maximum shifted slightly eastward. High ILD
436 location and ocean heat content are related to ENSO. Heat content of the Niño3 and
437 Niño3.4 zones showed an increasing trend, especially in latter, which also explains
438 increased probability of El Niño Modoki and the accumulation of energy in zone
439 Niño3.4. All the above results are consistent with the results of EOF analysis. In the
440 intersection area, there is a general correlation between each radiation flux and ENSO
441 related variables, such as west wind anomaly, ascending movement and heat content.
442 After the lead-lag correlation calculation, correlations between radiation and other
443 ENSO related variables such as u, w were generally enhanced.

444 3. Causality analysis showed a common causal relationship between radiation flux
445 and ENSO related variables, some of which are directly causal and some indirectly
446 related. Generally, radiation flux changes can affect changes in ocean heat, and these
447 can affect atmospheric circulation, which leads to a causal relationship between
448 radiation fluxes and ENSO related variables.

449 4. Changing trends in SDLR, SDSR and Niño3.4 index were similar, and
450 correlation coefficients of SDLR and Niño3.4 index and SDSR and Niño3.4 index

451 reached 0.3328 and 0.6255, respectively, which further verified the conclusion that the
452 probability of El Niño Modoki occurrence increased.

453 Long-term ENSO change is an important subject, and its influencing factors are
454 diverse. There are still many related physical variables and the role between them and
455 ENSO is worthy of further research. Currently, the variables related to ENSO we
456 considered, such as radiation flux and heat content, are also worthy of further research,
457 to achieve a deeper understanding of long-term ENSO changes.

458

459 **Data availability statement:**

460 The data that support the findings of this study will be openly available following an
461 embargo at the following URL/DOI: <https://doi.org/10.5061/dryad.xksn02vhk>.

462

463 **6. Reference**

- 464 [1]Meehl, G. A., Arblaster, J. M., Branstator, G., & wan Loon, H. (2008). A Coupled
465 Air - Sea Response Mechanism to Solar Forcing in the Pacific Region, *Journal of Climate*,
466 21(12), 2883-2897. Retrieved Jun 15, 2021.
- 467 [2] Haigh J D. The Impact of Solar Variability on Climate[J]. *Science*, 1996, 272(5264):981-984.
- 468 [3] Huo W J, Xiao Z N. The impact of solar activity on the 2015/16 El Niño event[J]. *Atmospheric*
469 *and Oceanic Science Letters*, 2016, 9(6): 428-435.
- 470 [4] Hu Z, Mcphaden M J , Kumar A , et al. Uncoupled El Niño Warming[J]. *Geophysical Research*
471 *Letters*, 2020, 47(7).
- 472 [5]Seiki Ayako, Takayabu Yukari N, Yasuda Tamaki, et al. Westerly wind bursts and their
473 relationship with ENSO in CMIP3 models[J]. *Journal of Geophysical Research*. 2011,116: D03303.
- 474 [6] Shi Yunhao Role of westerly burst in ENSO evolution [D] Chinese Academy of
475 Meteorological Sciences, 2020
- 476 [7] Wang song, Su Jie, Chu min, et al BCC_ CSM simulation of Arctic sea ice: comparison of
477 cmip5 and cmip6 historical tests [J] *Acta Oceanographica Sinica*, 2020, v.42 (05): 53-68
- 478 [8]Muñoz Sabater, J.: ERA5-Land monthly averaged data from 1981 to present [J]. Copernicus
479 Climate Change Service (C3S) Climate Data Store (CDS), 2019.

480 [9] Wu Xiaofen, Xu Jianping, Zhang Qilong, et al Cseof analysis of upper ocean heat content
481 in tropical western Pacific [J] Journal of Tropical Oceanography, 2011, 30 (6). 1
482 [10] Chen Shengjie, he Jinhai, Wu Zhiwei A new El Ni ñ o air sea coupling index [J]
483 Atmospheric science, 2013, 37 (4): 815-828
484 [11] Liang X S. Information flow and causality as rigorous notions ab initio[J]. Physical Review
485 E, 2016, 94(5):052201-1-28.
486 [12] Liang X S. Normalized Multivariate Time Series Causality Analysis and Causal Graph
487 Reconstruction[J]. Entropy, 2021, 23(6):679.
488 [13] Xz A, Sc A, Rjgb C , et al. Role of thermocline feedback in the increasing occurrence of
489 Central Pacific ENSO - ScienceDirect[J]. Regional Studies in Marine Science, 2020, 41.
490 [14] Ashok K, Behera S K, Rao S A, et al. et al. El Niño Modoki and its possible
491 teleconnection[J]. Journal of Geophysical Research Oceans, 2007, 112(C11):C11007
492 [15] Sang-Wook Yeh, Jong-Seong Kug, Boris Dewitte, et al. El Niño in a changing climate[J].
493 Nature, 2014, 461(sep.24):511-514.
494 [16] Weng H, Ashok K, Behera S K, et al. Impacts of recent El Niño Modoki on dry/wet
495 conditions in the Pacific Rim during boreal summer[J]. Climate Dyn,2007, 29(2/3):113-129
496 [17] Shen Xinlu, Wang Sihai Research progress of El Niño Modoki characterization index [J]
497 Modern agricultural science and technology, 2018 (15): 1
498 [18] Moum J N, Szoeki S D, Smyth W D, et al. Air – Sea Interactions from Westerly Wind
499 Bursts During the November 2011 MJO in the Indian Ocean[J]. Bulletin of the American
500 Meteorological Society, 2014, 95(8):1185-1199.
501